A new method for producing polylactic acid biocomposites for 3D printing with improved tensile and thermo-mechanical performance using grafted nanofibrillated cellulose

Christian Gauss[a*], Kim L. Pickering[a]

Abstract

In this work, a novel methodology was developed to disperse nanofibrillated cellulose (CNF) in polylactic acid (PLA) composites for 3D printing. The nanofibres were modified by grafting PLA onto their surface through in-situ polymerisation of L-lactide. This modification changed subsequent fibre/PLA interaction and enabled the production of reinforced microparticles by a Pickering emulsion approach. We demonstrated that filaments produced with these microparticles containing up to 20 wt% of grafted CNF (g-CNF) can be processed and printed using the same printing parameters as used for neat PLA. The printed samples presented superior tensile properties, enhanced thermo-mechanical stability, and were dimensionally stable upon PLA crystallisation when g-CNF content is above 10%. When heat-treated after printing the composite with 10% of g-CNF achieved an ultimate tensile strength and Young's modulus of 72 MPa and 5.4 GPa, respectively. Post printing annealing also increased thermo-mechanical stability of the composites achieving a storage modulus at 80 °C up to 850 times the storage modulus of neat PLA at the same temperature.

Keywords: Nano cellulose; Natural fibre; Additive manufacturing; Surface modification; Composite

* Corresponding author: cgauss@waikato.ac.nz

[a] School of Engineering, Division of Health, Engineering, Computing & Science, The University of Waikato, Private Bag 3105, Hamilton, New Zealand

1. Introduction

Additive manufacturing (AM), or three-dimensional (3D) printing, has become an attractive fabrication technology because it allows the direct and integrated production of complex and customised geometries using different materials (polymers, composites, ceramics, and metals) without the hurdles associated with large manufacturing facilities [1–3]. Of all the AM technologies, material extrusion methods, in special Fused Deposition Modelling (FDM) or Fused Filament Fabrication (FFF), are the most widely used methods for the manufacturing of prototypes and common parts [4,5]. With continuous demand for innovation in sustainable materials with a circular economy perspective, there is an increase in the interest and use of bio-derived materials in AM [3]. Polylactic acid or polylactide (PLA), for example, is a versatile and common feedstock material for FDM. It is produced from renewable resources, is biodegradable (under certain conditions), has good mechanical properties, and can be used in the formulations of composites reinforced with a wide range of natural fibres [6].

A large amount of work has been devoted to the understanding of cellulose properties for applications in biocomposites, especially the ones based on PLA [3,7–14]. The unique intrinsic mechanical properties of nano cellulose fibres, however, have not been fully translated into high-performance thermoplastic composites, regardless of manufacturing methods. The main issues in this regard are related to the limited compatibility between the hydrophilic cellulose fibres and hydrophobic thermoplastic matrices, resulting in poor fibre/matrix interface and heterogeneous dispersion. Nevertheless, cellulose nanofibres in general have demonstrated great potential as reinforcement for PLA filaments used in FDM [11,13–19]. When fibre-reinforced thermoplastics are used, the selective deposition of each layer in a defined printing direction/angle combined with fibre alignment induced in the nozzle during printing can be used to produce selectively reinforced structures. Although in general promising results are reported in the literature, the amount of nanofibres that can be successfully dispersed in the PLA matrix without causing problems with the printing process or negatively affecting the mechanical properties of the composites is very limited. In most cases, the content of nanofibres ranges from 1-5 wt [13,17–19]

Cellulose fibres (in the form of micro or nanofibres) have a large number of available hydroxyl groups involved in intramolecular (within cellulose polymeric chain) and intermolecular (between different molecules) bonding [20]. This characteristic of cellulose enables the grafting (bonding of

superficial molecules) with other functional groups onto cellulose's surface, which results in new properties/functionalities and is often used as a strategy to improve the cellulose/thermoplastic interface. One of the most common processes of grafting is to use a "grafting-from" approach to create a chemical bond between a polymer and cellulose. In this method, a monomer is polymerised in the presence of cellulose where the polymerisation process starts on the hydroxyl groups of cellulose [20]. An example of such process is the polymerisation of L-lactide in the presence of cellulose, forming PLA oligomers grafted onto the cellulose surface [21]. This process has shown promising results in terms of mechanical, thermal, and physical properties of PLA-based composites reinforced with nano cellulose [22–24]. In general, two possibilities for modification of nanoparticles using L-lactide are available: bulk reaction [24–26], where L-lactide in a molten state is polymerised into PLA in the presence of nanoparticles/fibres and solvothermal reaction, where the polymerisation is conducted in a solvent [21,27,28].

Besides cellulose surface modification, other approaches have been investigated to improve the dispersion of cellulose nanofibres in thermoplastics. It has been demonstrated that cellulose nanofibres, as nanofibrillated form or nanocrystals, can be used in Pickering emulsions, e.g. emulsions stabilised by nanoparticles, to stabilise apolar and hydrophobic phases containing a polymer (or monomer) in an aqueous medium containing hydrophilic cellulose [17,29–31]. In this concept, the cellulose nanofibres are adsorbed onto the interface between the two immiscible phases and work as an emulsion stabiliser [17]. By using TEMPO oxidised bacterial cellulose, for example, Li et al. 2019 produced PLA-based composites through a Pickering emulsion approach and processed them into filaments for 3D printing. The addition of TEMPO-oxidised BC improved tensile strength, bending strength, and Young's modulus by 9.2%, 45%, and 49%, respectively. The use of similar approach was used in a variety of nanocomposites [30–32]. Nonetheless, the effect of cellulose surface modification on the emulsification process with thermoplastics has not been comprehensively studied.

As a strategy to obtain PLA-based composites with improved mechanical performance, the main objective of this study was to develop a novel method to reinforce PLA based on the modification and dispersion of nanofibrillated cellulose (CNF). First, the fibre/matrix interface was improved by modifying nanocellulose fibres through *in situ* polymerisation of L-lactide, grafting hydrophobic functional groups onto cellulose's surface. Then, uniform dispersion of nanocellulose fibres was achieved using a modified Pickering emulsion approach where an aqueous suspension of grafted CNF (g-CNF)

suspension and PLA dissolved in dichloromethane were processed into g-CNF/PLA microparticles. It was hypothesised that the surface modification would change the emulsification behaviour and facilitate the dispersion of CNF in PLA. In the last phase, the obtained microparticles were melt-compounded with neat PLA, adjusting the grafted CNF content, and extruded into filaments that were used in fused deposition modelling. The obtained filaments and 3D printed samples were characterised by mechanical testing, dynamic mechanical analysis, microscopy analyses, and X-ray diffraction. Post printing annealing was also investigated as a way to improve the thermo-mechanical stability of these bio-composites.

2. Methodology

2.1. Materials

Freeze-dried cellulose nanofibrilated fibres (CNF) with a nominal fibre width of 50 nm were purchased from the University of Maine. The grafting reaction was performed using Purasorb L® L-lactide, purchased from Corbion. Polylactic acid (PLA) grade 2003D with MFI of 6 g/10 min (210°C, 2.16kg) and specific gravity of 1.24 g/cm^3 was purchased from NatureWorks® and used to produce the composites. Analytical grade Merck Millipore dichloromethane (DCM), toluene, methanol, and acetone were used during the process of grafting, cleaning, and PLA/CNF mixing.

2.2. CNF grafting

The CNF fibres were grafted through a solvothermal reaction, based on the methodology described elsewhere [21,23]. First, 5 g of CNF was dispersed in water using a 500W sonicator, centrifuged and solvent exchanged with acetone twice (re-dispersed after each step). The dispersed CNF in acetone was then added into a double-glass reactor with toluene at 80 ^{o}C and kept under stirring with nitrogen flow to evaporate the acetone in the system. L-lactide monomer (20 g) was dissolved in hot toluene and added to the reaction flask. After mixing, the catalyst $Sn(Oct)_2$ (2 wt% by monomer mass) was added to the reactor and the reaction was conducted for 24h under a nitrogen flow of 250 mL/min. After cooling, the obtained material was filtered and the solid fraction was washed thrice with DCM and ethanol to remove any ungrafted PLA and unreacted L-lactide. The modified fibres were filtered and dispersed in hot distilled water, centrifuged, and re-dispersed in a 1L volumetric flask with distilled water. This stock suspension had a concentration of approximately 0.5 % of g-CNF and was used for the production of PLA/g-CNF microparticles.

2.2.1. Characterisation of grafted CNF

A small batch of grafted CNF was produced using the same procedure and proportions of CNF, L-lactide, and $SnOct_2$ described above to determine the conversion degree of L-lactide and grafting yield. After finishing the reaction (24h), the reaction flask was cooled and the solution with CNF was precipitated in cold methanol obtaining a white solid. After a series of washing steps using methanol (centrifuge), the obtained precipitate was filtered and rinsed with ethanol thrice to remove any unreacted L-lactide. After drying at room temperature overnight, the obtained material was dried in a vacuum oven at 60 ^{o}C for 6 h. Then, the monomer conversion degree was calculated by gravimetrical method [22,33], according to the Equation 1:

$$C_g = \frac{A - B}{C} \times 100 \qquad (1)$$

Where C_g is the monomer conversion degree, B is the mass of orginal cellulose, A is the total mass obtained after the polymerisation reaction and cleaning steps, and C is the initial monomer fraction used in the grafting reaction.

The obtained solid was then dissolved in dichloromethane (DCM) to isolate the modified CNF for further analysis. This process was conducted by dissolving and separating the solid fraction by centrifugation (with two additional steps of cleaning with DCM). The extracted polymerised L-lactide was again precipitated in methanol for further analysis. The grafting yield was then calculated according to the Equation 2:

$$G = \frac{D - B}{B} \times 100 \qquad (2)$$

Where G is the grafting yield, D is the mass of grafted cellulose after washing (extracting the free polymer and monomer), and B is the mass of original cellulose.

The obtained modified fibres, named g-CNF (the fibres produced according to section 2.2) were characterized through infrared spectroscopy (FTIR), thermogravimetric analysis (TGA), and X-ray diffraction (XRD). For the FTIR analysis, dry g-CNF and CNF without modification (vacuum dried at 60 ^{o}C) were mixed with KBr, pressed into 10 mm discs and analysed in a PerkinElmer® Spectrum 100. For each analysis, 32 scans were used in the spectral region of 4000-600 cm^{-1} with a resolution of 4 cm^{-1}. The same fibres were also characterised in a Netzsch® STA449 F5 Jupiter thermogravimetric analyser from

30 to 600 °C at a heating rate of 10 °C/min under argon flow of 40 mL/min. An X-ray diffractometer (Panalytical Empyrean, with CuKα radiation generated at a voltage of 40 kV and a current of 40 mA) was used to scan the CNF samples between 5–65° 2θ using a step size of 0.01 ° and exposure of 40s. The crystallinity of cellulose, *CrI*, was calculated using the Segal peak height method [34], according to the following equation:

$$CrI = \frac{I_{002} - I_{am}}{I_{002}} \times 100 \qquad (3)$$

Where I_{002} represents the maximum intensity of the (002) plane reflection of the cellulose I structure at approximately 2θ = 22.7° and I_{am} is the intensity of the amorphous reflection at 2θ = 18°. The Zeta potential of the fibres were measured in a Mütek SKP 06 Zeta potential analyser using a 0.1 % aqueous suspension of unmodified CNF and grafted CNF. The samples were measured at the same temperature and suspension conductivity, which was adjusted to 0.460 mS/cm using a KCl stock solution.

2.3. Production of PLA/CNF microparticles through a Pickering emulsion approach

For the production of PLA/g-CNF microparticles, the suspension with g-CNF in water was mixed with a 10% (wt/V) solution of PLA in DCM in a proportion of 5:1 in volume (360 mL of g-CNF in water: 72 mL of PLA in DCM). In this formulation, the dry content of g-CNF in relation to PLA was 20%. The g-CNF/PLA mix was then sonicated for 8 min at cycles of 30s on and 5s off using a 500W QSonica sonicator with a 25.4 mm horn. An amplitude of 100% was used during the process, and the temperature was controlled using cold water. A control using unmodified CNF was also produced using the same concentration and procedure. After sonication, the resulting slurry with PLA/g-CNF microparticles was mixed continuously using a magnetic stirrer and left in a fume hood to evaporate the DCM overnight. After the sonication and after evaporating the solvent, small samples were extracted from the suspension and analysed in an Olympus (model BX53) optical microscope to evaluate the morphology of the particles. The final slurry was vacuum filtered and vacuum dried at 60 °C for 24h. The obtained material was then deagglomerated using a kitchen coffee grinder with a blunt blade, producing g-CNF/PLA particles, hereafter named PE-g-CNF. These particles were also analysed in a Hitachi S-4000 field emission scanning electron microscope (SEM), operated at 5 kV. The samples were mounted with carbon tape on aluminium stubs and then sputter-coated with palladium to make them conductive before SEM observation.

2.4. Filament production and characterisation

The obtained microparticles produced by the Pickering emulsion approach were melt compounded with neat PLA using a custom-made Sigma blade type compounder at 180 °C for 10 min (until the measured torque became constant) according to the composition shown in Table 1. After the first melt compounding, the composites were granulated into 3mm particles using a Moretto GR knife mill and extruded into filaments using a Filabot EX2 single screw extruder at 180 °C. The extrusion and pooling speeds were adjusted to produce filaments with a constant diameter of 1.70 ± 0.1 mm. A control filament with 10% of unmodified CNF (CNF_10) was also produced using the same processing conditions.

Samples extracted from the filaments were characterised in a Netzsch® STA449 F5 Jupiter thermogravimetric analyser from 30 to 600 °C at a heating rate of 10 °C/min under argon flow of 40 mL/min. The fracture surface of the filaments was also analysed in a Hitachi S-4000 field emission scanning electron microscope (SEM), operated at 5 kV. The samples were mounted with carbon tape on aluminium stubs and then sputter-coated with palladium to make them conductive before SEM observation.

Table 1 – Formulations of g-CNF/PLA composites and corresponding mass of g-CNF, PLA, and PE-g-CNF used

Condition	Nominal g-CNF content (wt%)	Total g-CNF mass (g)	Total PLA mass (g)	PE-g-CNF content (g)	Neat PLA (g)
PLA	0	0	50	0	50
g-CNF_1%	1	0.5	49.5	2.5	47.5
g-CNF_2%	2	1.0	49.0	5.0	45.0
g-CNF_3%	3	1.5	48.5	7.5	42.5
g-CNF_10%	10	5.0	45.0	25.0	25.0
g-CNF_20%	20	10.0	40.0	50.0	-

2.5. 3D printing

Samples for tensile testing, dynamic mechanical analysis (DMA), and X-ray diffraction (XRD) were 3D printed in a MakerGear™ M2 desktop 3D printer using the Simplify 3D® software package for slicing the .stl files and controlling the 3D printer. All the samples were printed with 100% infill density

using a nozzle of 0.35 mm, raster angle of 0º, layer height of 0.1 mm, bed temperature of 70 ºC, nozzle temperature of 210 ºC, and printing speed of 1800 mm/min. After printing, part of the samples were heat-treated at 105 ºC for 2 h. All the samples were then conditioned in a climatic chamber at 23 ºC and relative humidity of 50% for 48 h before further testing.

2.5.1. Characterisation of 3D printed composites

Tensile testing of the 3D printed samples was conducted on an Instron® 5982 tensile tester equipped with a 5 kN loadcell using a 10 mm extensometer at a crosshead displacement of 2 mm/min. ASTM D638 – V testing standard was used with free-span nominal dimensions of 3.18 mm, 1.20 mm and 10.96 mm for width, thickness and length, respectively. Five samples per condition were tested. The mechanical testing results were analyzed in the statistical software Minitab® 18 using one-way analysis of variance (ANOVA) test. The significant differences among averages were calculated using Tukey's method with a 95% of confidence.

Dynamic thermomechanical analyses were conducted in a Perkin Elmer DMA800 using single cantilever mode. Prismatic (5 x 1.5 x 30 mm^3) samples were 3D printed using the sample printing parameters of the tensile test specimens. The samples were tested between 22-140 ºC at 2 ºC/min using a frequency of 1 Hz and displacement amplitude of 50 µm.

The 3D printed samples were also characterised through Differential Scanning Calorimetry (DSC) analysis. Small samples of 9-12 mg were extracted from the specimens and analysed in a Netzch DSC3500 Sirius differential scanning calorimeter using aluminium crucibles from 20-200 ºC at 10 ºC/min with Nitrogen flow of 60 mL/min. The obtained scans were used to determine glass transition (Tg), melting (Tm), and cold crystallisation (Tcc) temperatures. The PLA crystallinity of the samples was determined according to Equation 4 [35]:

$$\boldsymbol{X_c = \frac{(\Delta H_m - \Delta H_{cc})}{\Delta H_f \times X_{PLA}}.100} \qquad (4)$$

where ΔH_m and ΔH_{cc} are the enthalpies of melting and cold crystallisation, respectively, ΔH_f is the melting enthalpy of 100% crystalline PLA (93 J/g) [35], and X_{PLA} is the weight fraction of PLA in the composite.

The effect of printing on the fibre orientation was investigated through XRD analysis. Disk samples of the g-CNF_20% formulation were 3D printed using raster angles of 0º (all the layers) and 0º/90º (alternate layers). The samples were then analysed in a Panalytical Empyrean XRD in transmission

mode using CuKα radiation (40 kV; 40mA) and a PixCel linear detector. First, the samples were analysed in a continuous 2θ scan mode between 5–45° 2θ using a scanning step of 0.01° and equivalent exposure time of 40 s at φ angles (disc rotation axis) of 0° and 90°. Then, a scan through the φ axis (0-180°) was conducted at the 2θ angle (approximately 21.2°) determined in the first scan using a step size of 0.5° and exposure time of 10s.

Micrographs of the fracture surface of the 3D printed samples were taken in a Hitachi S-4000 field emission scanning electron microscope (SEM), operated at 5 kV. The samples were mounted with carbon tape on aluminium stubs and then sputter-coated with palladium to make them conductive before SEM observation.

3. Results and discussion

3.1. CNF grafting

The production of grafted CNF (g-CNF) was carried out by ring-opening-polymerisation (ROP) of PLA initiated from the hydroxyl groups on the surface of CNF. This method results in stable grafted material on the surface of cellulose nanofibres which improves the compatibility with the PLA matrix. Preliminary experiments on the grafting reaction of PLA on the CNF fibres were conducted to determine the conversion degree of L-lactide into PLA and the grafting yield of the cellulose nanofibres using the proposed reaction parameters. The monomer conversion degree and grafting yield, calculated according to Equations 1 and 2, were 80.1% and 5.7%, respectively. The monomer conversion degree is in agreement with other studies that used a similar solvothermal reaction approach (70-83%) [21,22].

After the extraction, the obtained grafted CNF (g-CNF) and the L-lactide oligomer were analysed through FTIR and XRD. Figure 1 shows the FTIR spectra of grafted and ungrafted CNF and L-lactide oligomer (extracted from the polymerisation reaction). A highly pronounced peak at 1723 cm^{-1} on the g-CNF sample evidences the presence of carbonyl C=O functional group that is attributed to the grafted L-lactide oligomer. There is also a reduction in the intensity of the hydroxyl (-OH) peak at approximately 3600 cm^{-1}, which is expected when the polymerisation is initiated in this functional group. Similar results are reported in the literature [23,36]. A representation of the grafting reaction used in this study is given in Figure 1c. The modification of CNF also resulted in different dispersion behaviour in water, which was verified by Zeta potential analysis. The unmodified CNF had a Zeta potential of -32.5 mV, while a suspension with the grafted CNF presented a Zeta potential of -26.8 mV. This increase of the

Zeta potential value indicates a decrease in the aqueous suspension stability as a result of the addition of C=O functional groups on the cellulose surface.

The effect of grafting can also be seen in the XRD pattern of the modified CNF. There is a small increase in the diffracted intensity at 2θ=16.5 ºC in the grafted CNF, which is also the 2θ position of the highest peak of the L-lactide oligomer. The cellulose crystallinity index calculated using the Seagal method is 59% and 64% for the CNF and g-CNF, respectively. Figure 1b also shows the comparison between pure L-lactide monomer, commercial PLA (2003D), and L-lactide oligomer. The similarity between the oligomer and commercial PLA evidences that the polymerisation reaction was successful.

Additional characterisation of the grafted CNF (TGA) and L-lactide oligomer produced in the reaction (DSC and TGA) is available in the supplementary file (Figures S1 and S2).

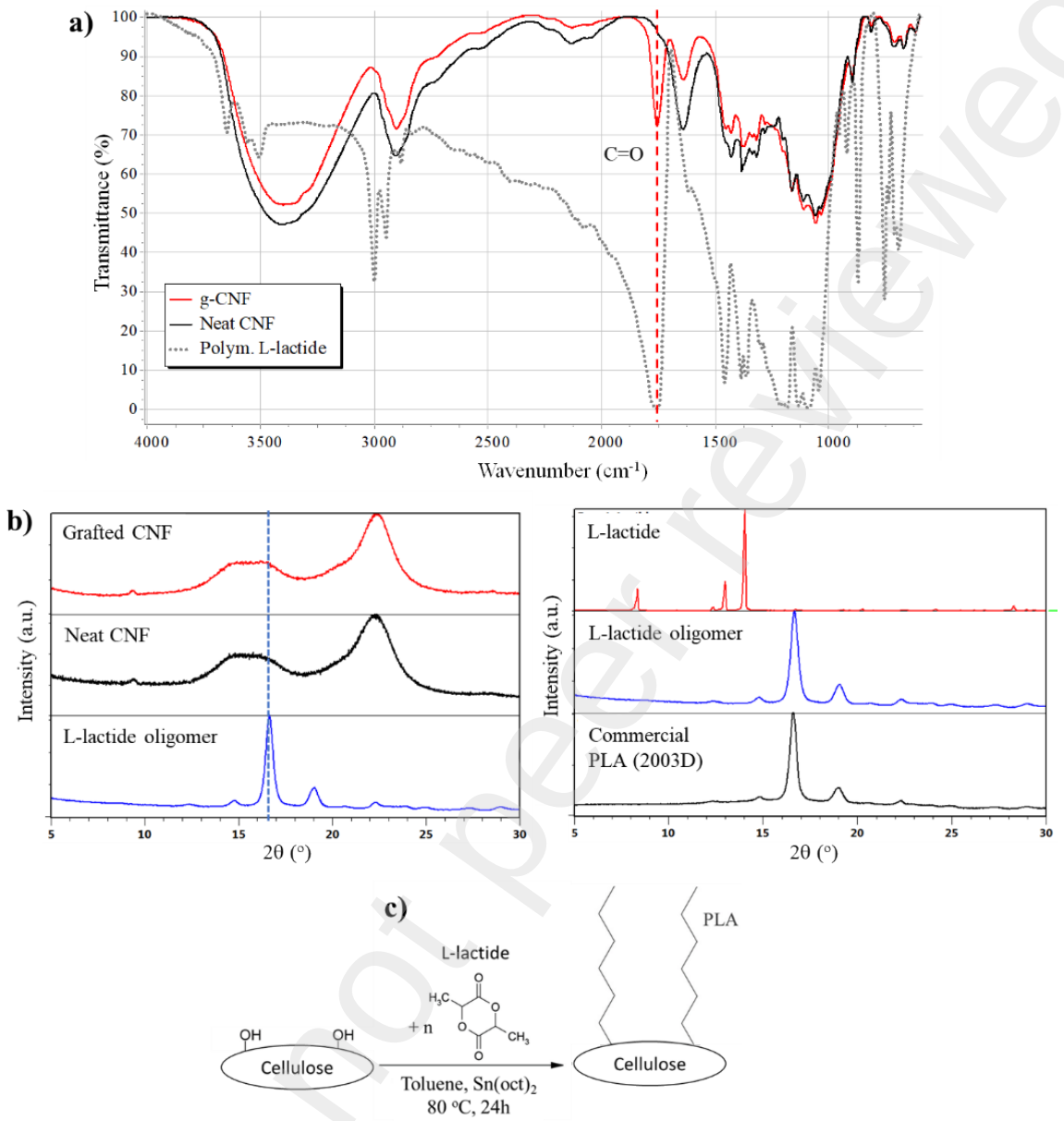

Figure 1 – a) FTIR spectra of neat CNF, g-CNF and L-lactide oligomer obtained in the solvothermal reaction. b) XRD results of the g-CNF and neat CNF (top image) and L-lactide oligomer in comparison to a commercial PLA (bottom). c) representation of the grafting reaction.

3.2. Production of g-CNF/PLA microparticles

Nanoparticles and nanofibres can be used to stabilise emulsions of immiscible phases (like oil and water) in a process called Pickering emulsion. Although this approach is applied mainly in the food industry, it also has been applied in the processing of composites based on nano cellulose [17,29–31]. In this case, the nano cellulose (as nanocrystals or nanofibres) is adsorbed onto the interface between two

immiscible phases, i.e. the aqueous cellulose suspension and a polymer or monomer dissolved in a nonpolar solvent, creating a stable emulsion [17]. Using this concept, we used the grafted CNF and unmodified CNF to produce PLA microspheres. The function of CNF was twofold in this case: work as an emulsion stabiliser and as reinforcement of PLA. The step-by-step process, from the sonication up to the final PLA/CNF microparticles, is summarised in Figure 2. When the CNF suspension and dissolved PLA are mixed and manually stirred, 2 phases are visible (Figure 2a). After a sonication treatment at an amplitude of 100% (500 W) for approximately 8 min, a stable emulsion was formed, with no identifiable phase interface. The resulting emulsion was left at room temperature under a fume hood to evaporate the DCM. After the evaporation of DCM, it was possible to filter the emulsion and obtain the microparticles shown in Figure 2d.

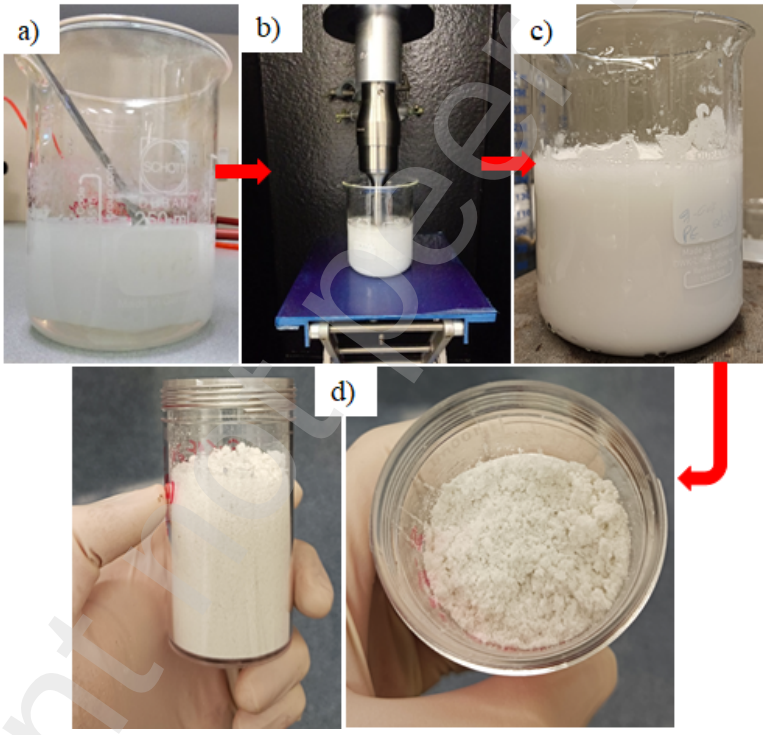

Figure 2 – PLA/water emulsion stabilised with CNF and g-CNF: a) before sonication and b-c) during and after sonication; d) g-CNF/PLA microparticles after filtering and drying.

The behaviour of the emulsification process using unmodified and grafted CNF was different. When unmodified CNF was used, a typical Pickering emulsion is formed, characterised by PLA microspheres encapsulated by CNF in an aqueous suspension of cellulose nanofibres. However, when grafted CNF was used, agglomerated microparticles of PLA/g-CNF are formed and most of g-CNF fibres had become incorporated. In addition, the mixing process using sonication was faster when g-CNF was

used, e.g. shorter sonication time is necessary to achieve a uniform suspension. This effect is explained by the increased affinity of the g-CNF with the apolar phase (dissolved PLA), which makes the fibres not stay only on the interface between the polar and apolar phases (as typically occurs in Pickering emulsions), but form micro agglomerates with dissolved PLA in a water medium. These effects can be observed in the optical and SEM images shown in Figure 3.

Droplets of the emulsion (just after sonication) produced using neat CNF and g-CNF were deposited over a microscopy glass and analysed by optical microscopy in transmission mode. Figures 3a and 3c show the resulting microscopic microspheres (in the case of CNF) and microparticles (in the case of g-CNF). In the case of the CNF emulsion, it is possible to observe that part of the CNF was still present as a water suspension, while in the g-CNF emulsion, most of the fibres are agglomerated with PLA in the form of microparticles. In both cases, most of the particles had diameters below 50 μm.

After filtering the emulsion/suspension and drying, the obtained particles were analysed by SEM. Figure 3b shows the obtained PLA microspheres surrounded by cellulose nanofibres embedded in a CNF network, which is a common arrangement observed in Pickering emulsions using CNF [17]. On the other hand, in the microparticles produced using g-CNF (Figure 3d), it is possible to observe the CNF fibres but they are agglomerated with PLA in a different arrangement than the neat CNF counterpart. From a processing point of view, this is seen as advantageous since most of the fibres are already embedded in PLA before the compounding process used to produce the 3D printing filaments.

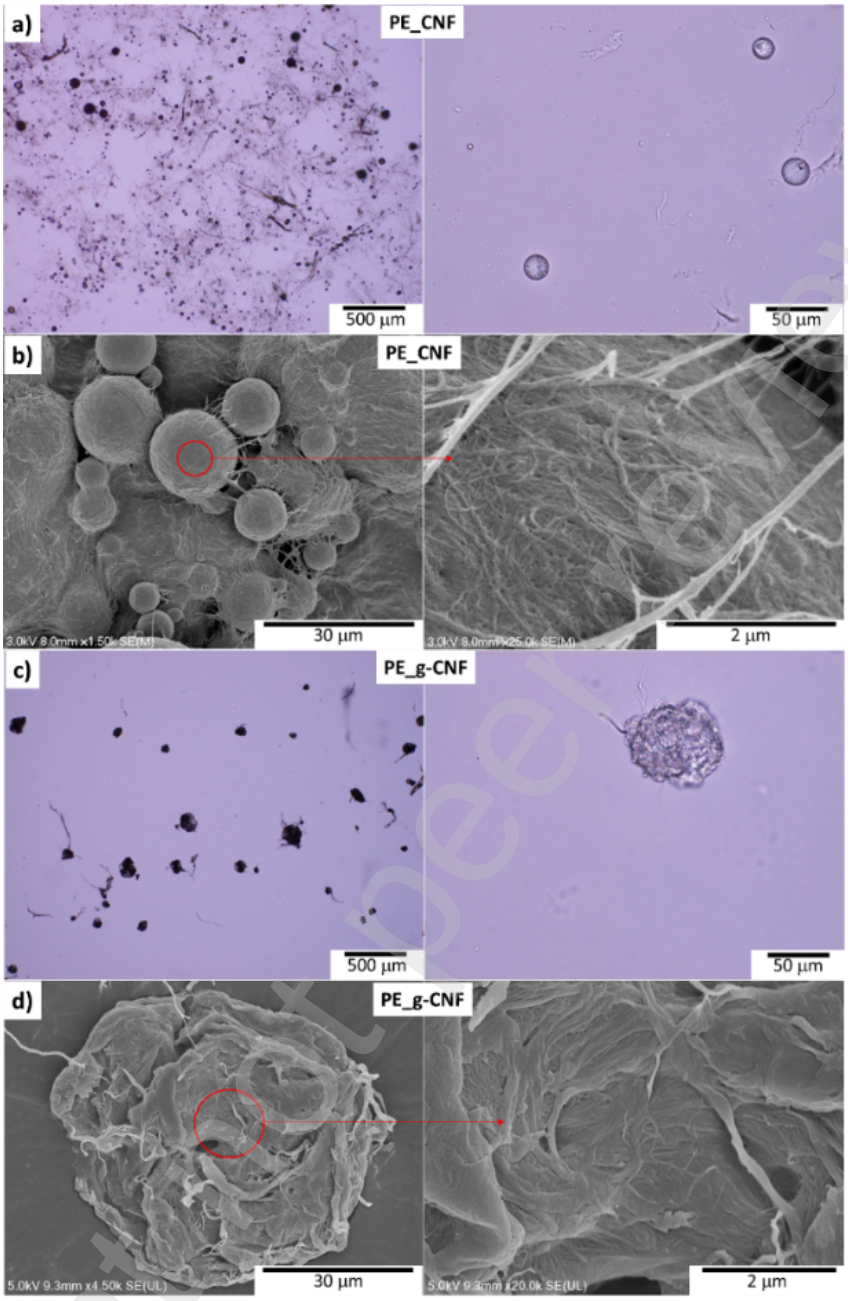

Figure 3 – SEM micrographs of CNF/PLA composite obtained by Pickering emulsion process. Optical microscopy images of the Pickering emulsion formed with unmodified CNF (a) and grafted CNF (c). SEM micrographs of dried CNF/PLA microspheres (b) and g-CNF microparticles (d).

3.3. Filament production and characterisation

Stereo optical microscopy images of filaments with 10 and 20 wt% of g-CNF are shown in Figure 4. Independently of the g-CNF content, all the filaments had similar diameters (1.70 ± 0.1 mm) and smooth surfaces, even the formulation with high g-CNF content (20 wt%). Surprisingly, the

composites with g-CNF were easily processed into filaments by the single-screw extruder using the same processing conditions of neat PLA. In fact, it was easier to control the filament diameter of the composite formulations than neat PLA. However, the behaviour of the composite with 10 wt% of unmodified CNF was different, and constant adjustment in the extrusion speed was necessary to obtain an appropriate filament. In addition, the surface of this formulation was rougher in comparison with the composite with g-CNF and agglomerates of fibres were visible, as shown at the bottom of Figure 4. Because of this problem, it was necessary to use a 0.75mm nozzle to print the samples of this formulation (for all the other formulations, a 0.35mm nozzle was used).

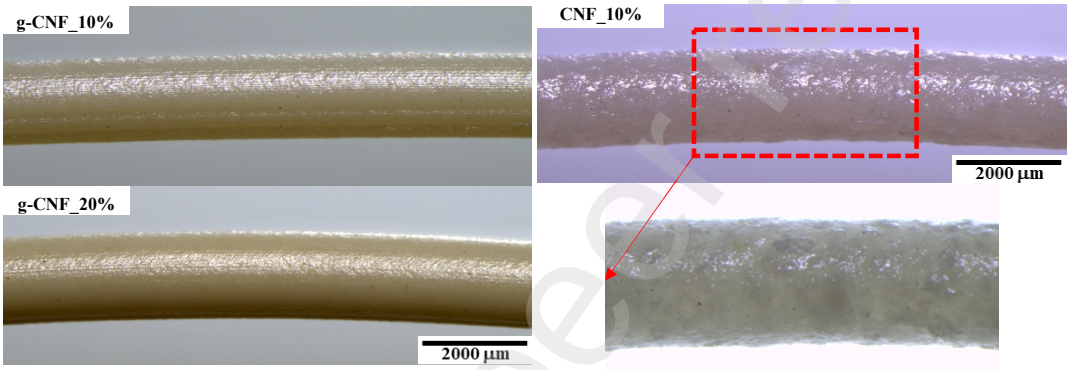

Figure 4 – Stereomicroscope images of filaments reinforced with g-CNF and CNF (on the right).

The filaments of neat PLA and the composites with 3 wt%, 10 wt%, and 20 wt% of g-CNF were thermally characterised using TGA analysis. Figure 5 shows the TG and DTG curves of these formulations and the corresponding onset temperature (T_{onset}), the temperature at 5% of weight loss ($T_{5\%}$), the temperature of maximum degradation rate (T_{max}), and residual weight at 600 °C are summarised in Table 2. There is a decrease in the onset temperature and temperature of maximum degradation rate with the addition of g-CNF. This effect is expected, considering the lower thermal stability of CNF and L-lactide oligomer in comparison to neat PLA, as shown in the TGA results in the supplementary file. The decrease in thermal stability in grafted CNF has also been observed elsewhere [23]. This effect is attributed to the low molecular weight of the L-lactide oligomer grafted on the surface of the CNF fibres. However, the decrease in thermal stability is minimal in comparison with neat PLA and the onset temperature of degradation is still much higher than the processing and printing temperatures used for these composites (between 180-210 °C).

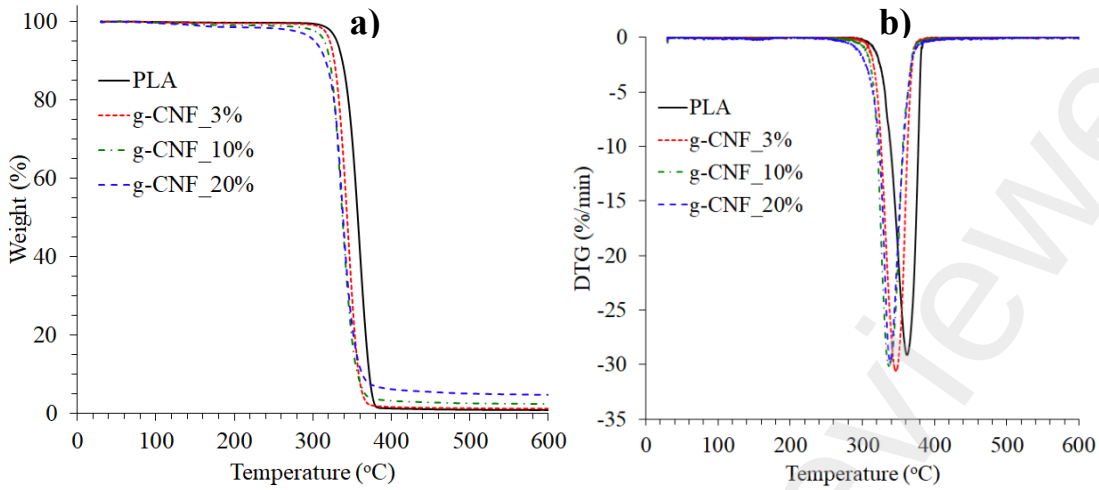

Figure 5 – TGA (a) and DTG (b) curves of neat PLA and g-CNF composite filaments.

Table 2 – Summary of TGA analysis of neat PLA and composite filaments.

Sample	T_{onset}	$T_{5\%}$	T_{max}	Residual weight (600 °C)
Neat PLA	339	330	362	0.78
g-CNF_3%	325	322	346	1.16
g-CNF_10%	320	315	336	2.36
g-CNF_20%	320	302	338	4.68

SEM images of fractured surfaces of filaments of neat PLA and g-CNF composites are presented in Figure 5. The filament samples were fractured under tensile loading at room temperature and all the samples were loaded using the same cross-head displacement rate. The test was performed only for microstructural characterisation purposes therefore the corresponding stress and strain were not recorded. Porosity, which is a problem often reported in cellulose-reinforced PLA filaments was not apparent [12,37]. In addition, the reinforced filaments have uniform fracture mode, similar to neat PLA, and well-distributed g-CNF. Up to 10 wt% of g-CNF, it was not possible to identify agglomerated fibres in the composites even using high magnification, evidence supporting good compatibility between the modified CNF and the PLA matrix. However, on the filament with 20 wt% of g-CNF, although it is not possible to differentiate the g-CNF fibres from the matrix, it is possible to observe a more heterogeneous and rougher fracture surface and voids (indicated by the red arrows) that are believed to be attributed to fibre pull-out.

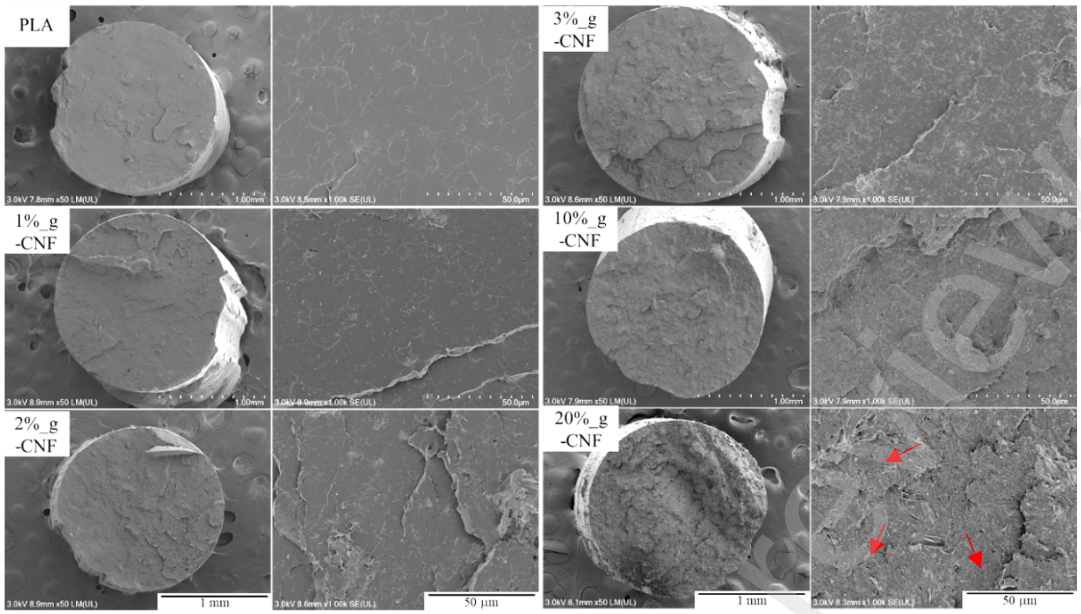

Figure 5 – SEM images of the fractured cross-section of neat PLA and reinforced filaments with 1-20 wt% of g-CNF. The red arrows indicate voids caused by the pullout of fibres.

3.4. 3D printing of PLA/g-CNF composites

All the filaments produced with g-CNF (between 1-20 wt%) had excellent processability and printability. The same processing and printing conditions used for neat PLA were used for all form formulations. In addition, even with high fibre loading, a small nozzle diameter could be used (0.35 mm) without any clogging problems during printing. The resulting quality of the printed samples can be seen in Figure 6. Even with 20 wt% of g-CNF, high dimensional and surface quality was achieved. Most studies on 3D printing of fibre reinforced composites use printing nozzles between 0.4-0.75 mm, which may limit the printing quality in some applications [14,19,38–40]. The filament with 10 wt% of unmodified CNF on the other hand, presented a pronounced surface roughness and CNF agglomerates (see Figure 4) which considerably affected its printability, making it necessary to use a 0.75 mm nozzle to successfully print the samples without nozzle blockage.

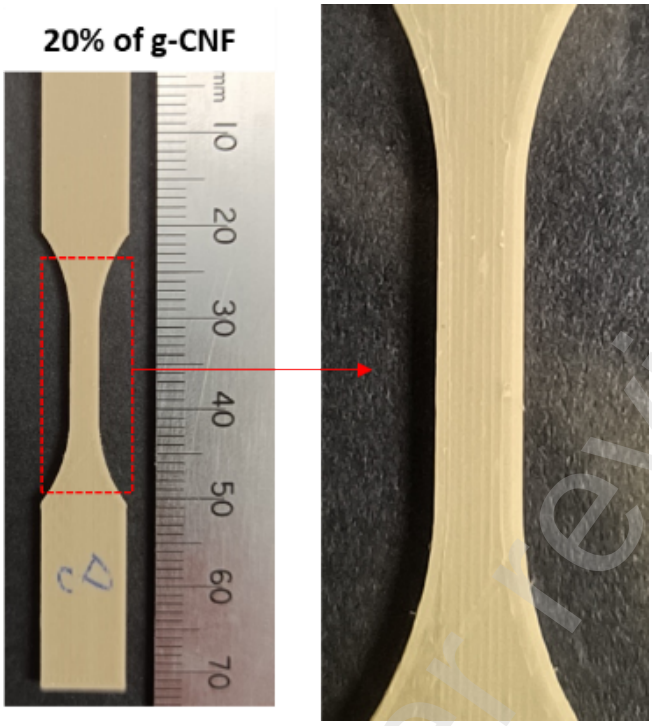

Figure 6 – Photograph showing the quality of g-CNF_20% 3D printed sample. The sample was printed with a 0.35 mm nozzle.

3.4.1. Tensile properties

The obtained tensile strength and Young's modulus of all the formulations are summarised in Figure 7. There is a gradual increase in Young's modulus up to a fibre loading of 20 wt%. The increase in tensile strength was less pronounced because it is more sensitive to defects and weak regions in composites creating stress concentration points. It is worth mentioning that the 3D printed neat PLA samples also had good tensile properties, which evidences the appropriate sample geometry and printing conditions used in this study. Even when reinforcing fibres are absent, the printing orientation in relation to the loading direction also has an important role in the final mechanical properties [41–44].

The highest tensile strength and Young's modulus was achieved by the g-CNF_20% formulation, 67 MPa and 5.8 GPa, respectively (see Table 3 for a summary of the results). Only 10% of g-CNF was enough to precisely 3D print composites with improved tensile properties; 66 MPa and 4.6 GPa for tensile strength and Young's modulus, respectively. These values are higher than the values reported in the literature for 3D printed short fibre reinforced PLA which vary between 15-57 MPa for tensile strength and 1-4.4 GP for Young's modulus depending on the fibre content and printing parameters [12,37,45–48]. The obtained values are also in the same range and even higher than 3D

printed PLA reinforced with synthetic short fibres such as glass and carbon fibres, which are reported to have tensile strength and Young's modulus between 44-60 MPa and 2.1-4.8 GP, respectively [49–51].

The effect of CNF modification can be seen clearly when we evaluate the mechanical performance of the composite with 10% of unmodified CNF (CNF-10 in Figure 7), which was produced using the same preparation (Pickering emulsion) and compounding process used in the g-CNF composites. Although there is an increase in Young's modulus with the addition of unmodified fibres, the tensile strength of printed CNF-10 formulation is lower than neat PLA and the g-CNF_10% composite, a behaviour often described in PLA-based composites with high content of CNF.

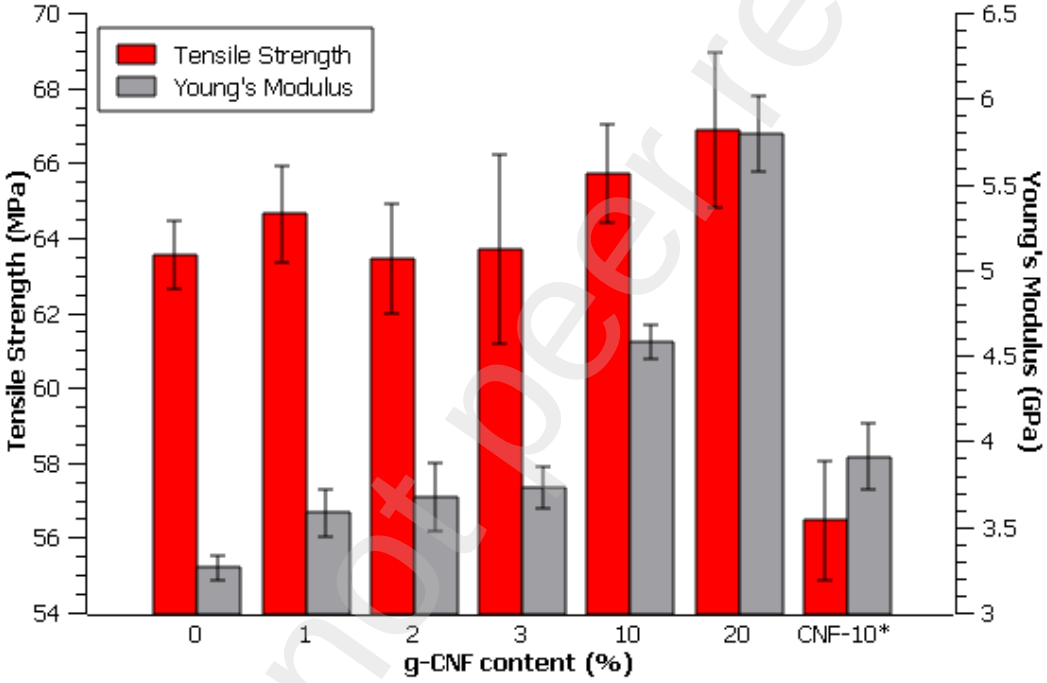

Figure 7 – Tensile properties of 3D printed composites with different content of g-CNF. * The sample CNF-10 has 10 wt% of un-modified CNF and was printed with a 0.75 mm nozzle (printing with 0.35 mm was not possible due to clogging issues). The error bars indicate one standard deviation.

The fracture surfaces of 3D printed PLA, g-CNF-1% and g-CNF-10% are shown in Figure 8. A typical fracture is observed in the neat PLA sample, where the different printing layers are visible and interlayer (inter-bead porosity) and inner-layer (inner-bead porosity) voids are present. The samples g-CNF-1% and g-CNF-10% have uniform fracture throughout the thickness and are more consolidated than neat PLA, i.e. they have lower inter-bead porosity. The sample with higher g-CNF content shows signs of

a brittle failure, but the fracture is uniform across the thickness and the different layers are indistinguishable.

Considering the nanoscale of the CNF fibres, it is not possible to visually analyse the alignment of the fibres in the printed samples. Therefore, XRD analysis was conducted to evaluate if the printing conditions induce fibre alignment in the printing direction. The resulting diffractograms are given in Figure 9. In Figure 9a, the 2θ scan of a sample printed with all the layers at 0^o shows that when the sample is rotated in the φ axis (around the central perpendicular axis of the disc) by 90^o there is a considerable change in the intensity of the peak at approximately $2\theta=22^o$, which is related to the (002) plane of cellulose I structure. Cellulose fibres have crystalline regions with specific orientation [52], and therefore, it is possible to estimate the overall fibre orientation in relation to a reference axis by tracking the change in intensity of diffracted X-ray of a specific plane with the change of a rotation axis. In this case, the (002) plane identified in the first 2θ scan was kept constant, and a second scan in the φ axis (azimuthal scan) was performed to determine the variation of diffracted intensity from 0-360^o. Figure 9b shows the resulting φ scan of two different samples; one of the samples was printed using a raster angle o 0^o in all the layers (red line) and the other sample was printed with alternate layers of 0^o and 90^o (blue line). The change in the diffracted intensity at the φ angles of 90^o and 270^o indicates that the cellulose nanofibres in the composite have a preferred orientation. This effect is better visualised when the sample printed at $0/90^o$ is considered. In this sample, the intensity throughout φ scan is more uniform with changes in intensity occurring every 90^o which is consistent with the printing angle difference between each layer. Therefore, the shear forces involved in the printing process were enough to partially align the cellulose nanofibres in the printing direction, which contributes to better mechanical properties when the applied load direction is parallel to the printing direction.

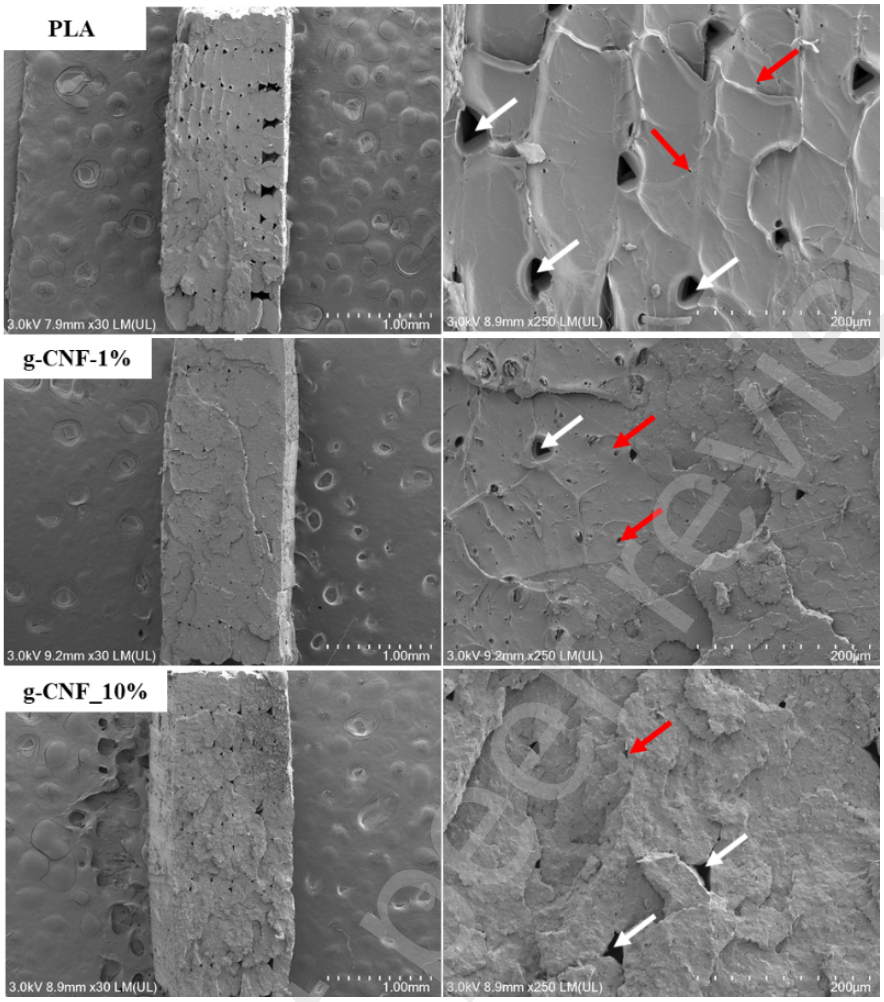

Figure 8 –SEM image of the fracture surface of 3D printed neat PLA and g-CNF_1% and g-CNF_10% composites. White arrows indicate inter-bead porosity and red arrows indicate inner-bead porosity.

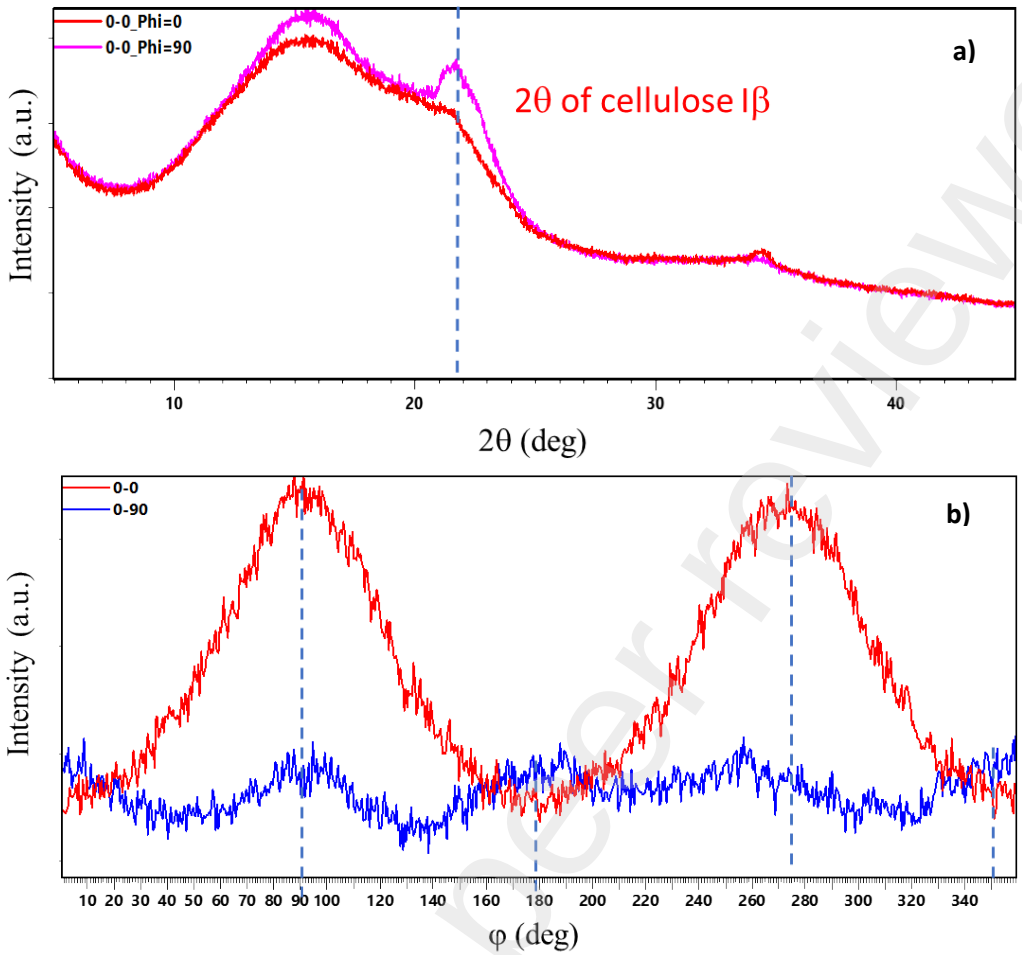

Figure 9 – XRD analysis of printed g-CNF_20% in transmission mode. The top XRD patterns (a) show the difference in the 2theta scan of the sample printed with raster angle of 0° analysed at the ϕ angles of 0° and 90°. The patterns in the bottom plot (b) show the change in intensity along the ϕ axis (0-360°) at a fixed 2θ angle (approximately 22°) of samples with all layers printed at raster angle of 0° (red line) and alternate layers of 0/90° (blue line).

3.4.2. Effect of post-printing heat-treatment

Post printing heat treatment was used to improve the thermo-mechanical properties of the g-CNF/PLA composites. The PLA grade used in this work (2003D) shrinks and warps with the increase in crystallinity and is not appropriate for heat treatment. However, when fibres are added this effect is minimised or completely absent which makes it possible to perform this kind of approach to improve the thermo-mechanical properties of the composites. This effect can be visualised in Figure 10, where tensile test samples with 1,3, and 10 wt% of g-CNF before and after heat treatment at 105 °C for 2h are shown.

There is a clear decrease in shrinkage in the printing direction with the addition of g-CNF. In the samples with 10 and 20 wt% of g-CNF, there was no dimensional change upon heat treatment. However, neat PLA and samples with 1 and 2 wt% of g-CNF were considerably distorted and could not be mechanically tested.

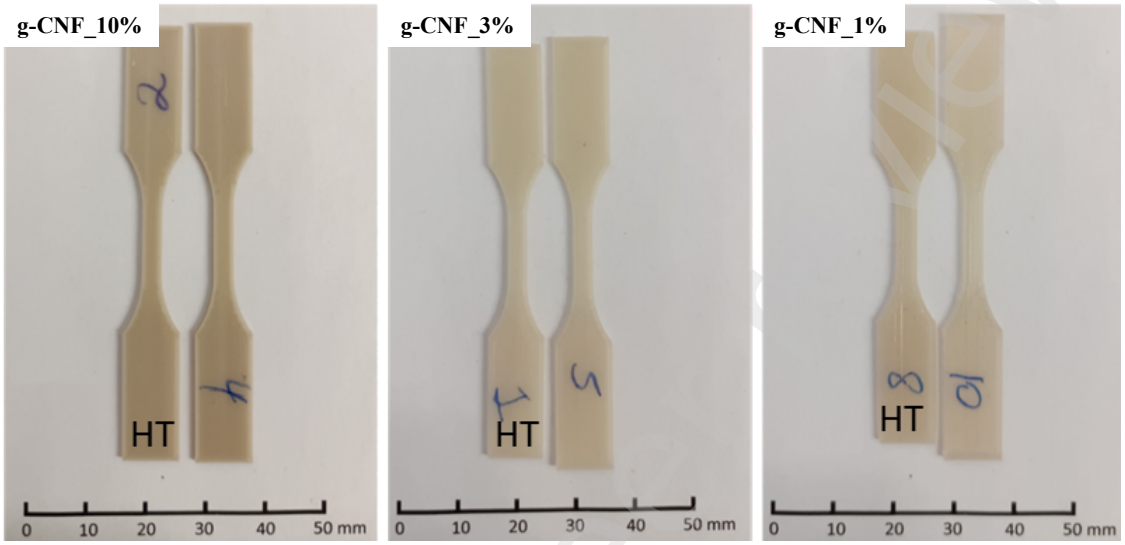

Figure 10 – Influence of heat treatment on the dimensions of 3D printed samples used for tensile testing. HT: Heat treated.

Table 3 gives the tensile testing results of the g-CNF composites before and after heat-treatment. As previously mentioned, there is a gradual increase in Young's modulus with the addition of g-CNF and a small increase in the tensile strength. However, the elongation at break of the composites is reduced with the addition of g-CNF, a behaviour often reported in 3D printed samples with CNF. With heat treatment, there was a considerable improvement in the ultimate tensile strength and Young's modulus of the composites in special the g-CNF_10% formulation, achieving a UTS of 72 MPa and E of 5.42 GPa, which is 10% and 18% higher, respectively, than the as-printed samples and 14% and 66% higher than neat PLA. To the best of our knowledge, these are the highest values reported for 3D printed PLA reinforced with 10 wt% of CNF. However, although the samples with 20 wt% of g-CNF had an improvement in Young's modulus with heat treatment, there was no positive effect on the UTS. This formulation presented a low value of elongation at break (1.05%) and small stress concentrations in the sample could have led to premature failure, affecting the UTS.

Table 3 – Summary of tensile properties of as-printed samples and heat-treated samples. Same letters (a to f) indicate that there is no statistical difference between formulations.

Formulation	UTS (MPa)		E (GPa)		ε_b (%)	
	Avg.	COV	Avg.	COV	Avg.	COV
As-printed						
Neat PLA	63.5^{c}	0.015	3.26^{f}	0.020	5.12^{a}	0.233
g-CNF_1%	64.6^{c}	0.020	3.58^{e,f}	0.038	3.65^{b}	0.241
g-CNF_2%	63.4^{c}	0.023	3.67^{e}	0.056	3.31^{b,c}	0.215
g-CNF_3%	63.7^{c}	0.040	3.73^{e}	0.033	2.72^{b,c,d}	0.137
g-CNF_10%	65.7^{c}	0.020	4.58^{d}	0.022	2.05^{c,d,e}	0.057
g-CNF_20%	66.9^{c}	0.031	5.79^{b}	0.038	1.39^{e}	0.125
Heat-treated						
g-CNF_3%-HT	70.7^{a,b}	0.025	4.49^{d}	0.040	2.06^{c,d,e}	0.052
g-CNF_10%-HT	72.2^{a}	0.020	5.42^{c}	0.033	1.62^{d,e}	0.049
g-CNF_20%-HT	64.7^{c}	0.059	6.55^{a}	0.031	1.05^{e}	0.045

Where UTS: Ultimate tensile strength; E: Young's modulus; ε_b: Elongation at break.

The improvement in the tensile properties with heat treatment is explained by the increase in PLA crystallinity and it is also hypothesised that there it improves the interfacial bonding between matrix and nanofibres. A summary of the DSC analysis of the 3D printed samples is given in Table 6 and the corresponding heating curves of some formulations are shown in Figure 11a. First, there is a gradual decrease in the cold crystallisation temperature with the addition of g-CNF in the as-printed samples. The g-CNF fibres work as nucleating agents for the crystallisation of PLA, decreasing the energy necessary to start the crystallisation. This effect can be better visualised in Figure 11b, where an isothermal scan at 105 ^{o}C (sample temperature used in the heat-treatment of printed samples) demonstrates the faster kinetics for crystallisation in the samples with 20% of g-CNF. In the neat PLA sample, approximately 60 min is necessary for heat flow stabilisation while for the samples with g-CNF less than 20 min is necessary. After 2 hours of heat treatement at 105 ^{o}C all the formulations, including neat PLA, had similar crystallinity varying between 25.8 – 27.6 %. The addition of g-CNF does not have an evident influence on the melting temperature or Tg determined by the DSC analysis.

Table 6 – Summary of first DSC heating cycle of as-printed and heat-treated samples.

Sample	Tg (°C)	Tcc peak (°C)	Tm peak (°C)	ΔHm (J/g_{PLA})	ΔHcc (J/g_{PLA})	X_c (%)
As-printed						
PLA	64.0	120.9	152.7	21.74	-18.65	3.38
g-CNF_1%	63.0	114.8	151.7	25.89	-24.37	1.62
g-CNF_2%	63.0	116.3	152.1	24.90	-22.97	2.07
g-CNF_3%	63.0	116.3	152.1	24.93	-23.73	1.56
g-CNF_10%	63.0	112.7	151.3	25.63	-22.83	3.01
g-CNF_20%	64.2	112.7	151.3	29.76	-22.71	6.74
Heat-treated						
PLA-HT	70.4	-	151.9	24.7	-	26.36
g-CNF_1%-HT	71	-	151.6	25.51	-	27.23
g-CNF_2%-HT	71.2	-	153	25.85	-	27.59
g-CNF_3%-HT	71.2	-	152	24.21	-	25.83
g-CNF_10%-HT	70.6	-	152.3	25.42	-	27.13
g-CNF_20%-HT	-	-	151.1	25.01	-	26.69

Tcc – Cold crystallisation temperature; Tg – Glass transition temperature; Tm – Melting temperature; ΔHcc – Cold crystallisation heat; ΔHm – Heat of melting; Xc – PLA crystallinity.

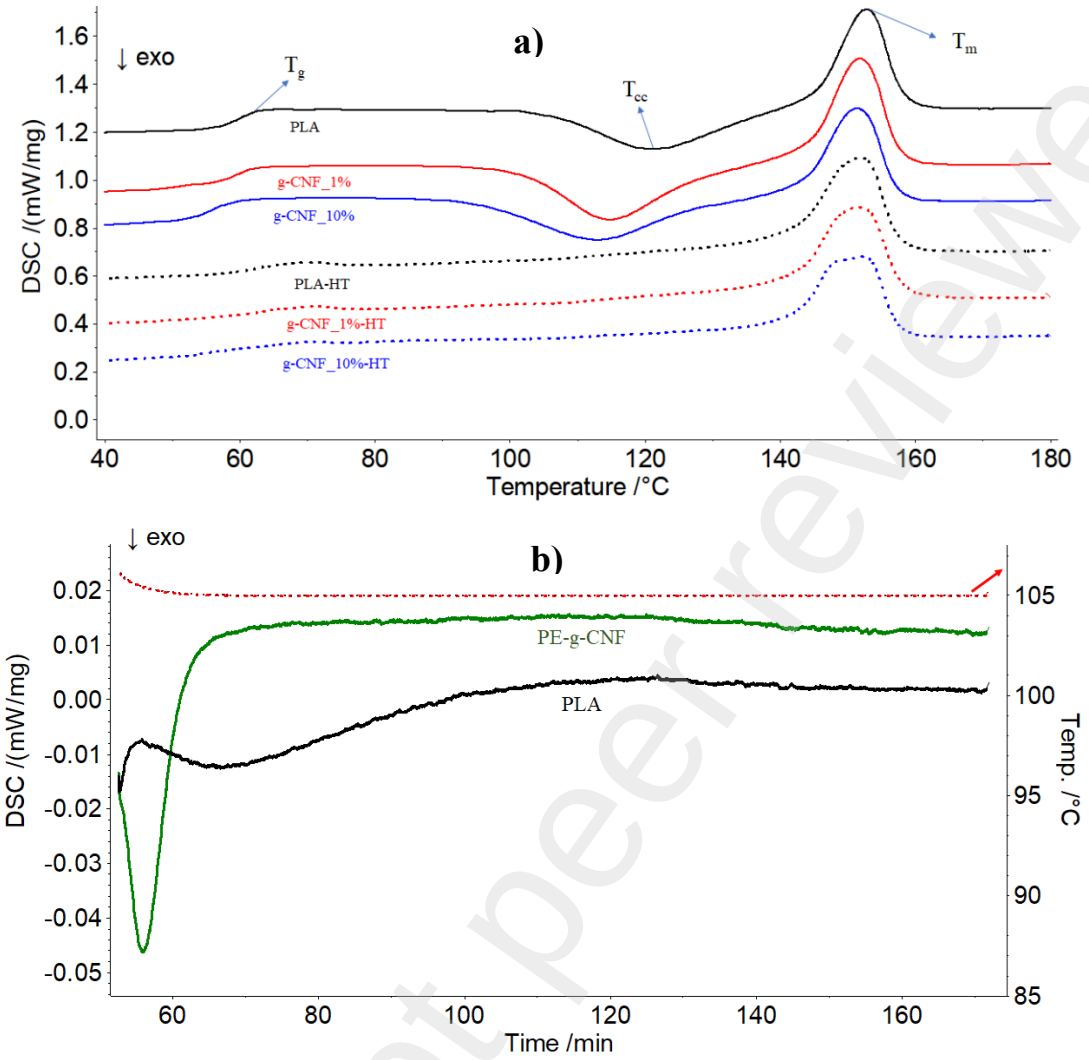

Figure 11 – a) DSC curves of as-printed and heat treated samples of neat PLA, g-CNF_1%, and g-CNF10%. T_g, $T_{cc,}$ and T_m refer to glass transition temperature, temperature of cold crystalisation, and temperature of fusion. b) Crystallisation behaviour of neat PLA and PE-g-CNF composite at isothermal scan at 105 °C.

3.4.1. Thermo-mechanical properties

Reinforcing PLA with fibres improves its thermo-mechanical stability, which can broaden its applications, especially when high gradients of temperature are present [14,53–55]. The use of nano fibres such as CNF has also been reported to have a positive effect on the thermo-mechanical stability of PLA, including improved storage modulus at higher temperatures and better creep resistance [14,56]. Therefore, DMA analysis was used to evaluate the thermo-mechanical stability of the 3D printed nanocomposites reinforced with g-CNF. Figure 12 presents the resulting storage modulus (E') and tan

δ of the as-printed and heat-treated samples in comparison with PLA. A summary of the obtained results, including the storage modulus at different temperatures, loss modulus peak (E'') temperature, maximum tan δ, and temperature of maximum tan δ, is given in Table 4. It is worth mentioning that, as mentioned in the tensile test section, only the samples heat-treated with 3, 10, and 20 wt% of g-CNF were tested. Neat PLA and other formulations had considerable shrinkage in the printing direction and could not be tested. In Figure 12a, it is possible to observe that the main influence of the addition of g-CNF is on the storage modulus at higher temperatures, especially after Tg. The nanofibres limit the mobility of PLA chains, improving the elastic component and decreasing the viscous behaviour of the composites, as can be seen by the decrease in the max tan δ, which is the ratio between loss modulus (E'') and storage modulus (E') and is used to identify the glassy to rubbery transition temperature (Figure 12c). In addition, as previously shown in the DSC results, the addition of g-CNF also decreases the temperature to start the crystallisation of PLA, which is evidenced by the increase in the storage modulus after approximately 90 ^{o}C. There is a decreasing trend in the temperature in which the composites start to have an increase in the storage modulus with the amount of added g-CNF (summarised in Table 4).

With heat-treatment after printing, and consequently with the increase in PLA crystallinity (see Table 6), there is a drastic improvement in the thermo-mechanical stability of the composites. Figure 12b and Figure 12d show the storage modulus and tan δ curves, respectively, of the heat-treated samples with 3,10, and 20 wt% of g-CNF. In addition to the influence of g-CNF in the improvement of thermo-mechanical stability, the presence of crystalline regions decreases the mobility of PLA molecules, which is translated into higher storage modulus at higher temperatures. The sample with 20 wt% of g-CNF, for example, had a storage modulus 17 times higher than neat PLA at 60 ^{o}C and at 80 ^{o}C it is 850 times higher. In fact, the storage modulus of this formulation at 60 ^{o}C is similar to that of neat PLA at 25 ^{o}C. The beneficial effects of heat-treatment can also be observed in the sharp decrease in the max tan δ values of the nanocomposites and increase in the tan δ peak temperatures, which is related to a much less pronounced glassy to rubbery transition and a predominance of elastic behaviour.

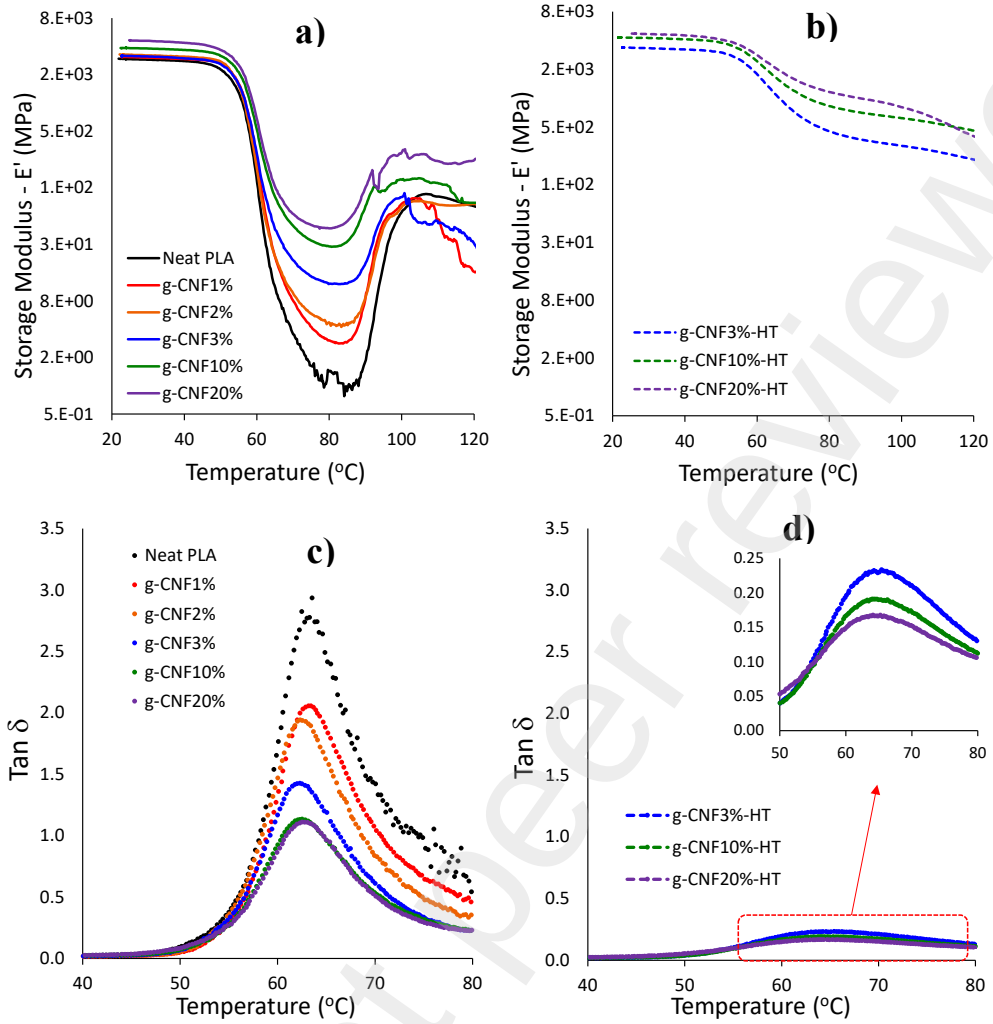

Figure 12 – Storage modulus (E') of all the formulations with g-CNF before (a) and after heat-treatment (b) and tanδ plots before (c) and after heat-treatment (d).

The effect of CNF grafting in comparison with unmodified CNF was also evaluated through the calculation of the effectiveness coefficient and adhesion factor. The effectiveness coefficient (C) can be calculated using the storage modulus of the composite and neat polymer in the glassy and rubbery regions, according to Equation 5 [57]; the adhesion factor (A) is calculated using the max tanδ values of the composite and neat polymer according to Equation 6 [58]. When there is high interfacial adhesion between the fibre (or filler) and matrix, the molecular mobility around the fibre is reduced and therefore, low values of adhesion factor suggest better interfacial bonding between fibre and matrix [58]. Similarly lower values of effectiveness coefficient generally infer better fibre/matrix interfacial bonding [57,59]. Table 5 shows the obtained results of 3D printed composites with 10 wt% of CNF and g-CNF. The

storage moduli at 25 °C and 80 °C of the composite with g-CNF are higher than those of the CNF composite and there is also a decrease in the max tanδ temperature. In addition, the lower values of effectiveness coefficient and adhesion factor of the g-CNF composite also indicate that the grafting modification improves the interfacial bonding between the nanofibres and PLA matrix, corroborating with the improved mechanical performance observed in the tensile tests.

$$C = \frac{\frac{E'_g}{E'_r}(composite)}{\frac{E'_g}{E'_r}(neat\ PLA)} \quad (5)$$

$$A = \frac{1}{(1 - \Phi_f)} \frac{tan\delta_c}{tan\delta_p} - 1 \quad (6)$$

Where C is the effectiveness coefficient, E'_g is the storage modulus in the glassy region (25 °C), E'r is the storage modulus in the rubbery region (80 °C), Φ_f if the fraction of fibres (g-CNF in this case), $tan\delta_c$ is the tanδ of the composite and $tan\delta_p$ is the tanδ of neat PLA.

Table 4 – Summary of DMA results of as-printed and heat-treated samples.

Condition	T_{ic} (°C)	E' 25 °C (MPa)	E' 60 °C (MPa)	E' 80 °C (MPa)	E" peak temp. (°C)	Max. Tan δ temp. (°C)	Max. Tan δ
As-printed							
PLA	90.7	3,001	170.1	1.416	56.0	63.6	2.94
g-CNF_1%	88.2	3,155	288.5	3.047	56.5	63.2	2.06
g-CNF_2%	87.8	3,344	240.2	4.736	56.2	62.3	1.94
g-CNF_3%	87.2	3,240	339.6	12.09	56.2	62.3	1.43
g-CNF_10%	83.2	3,938	581.9	30.57	57.0	62.5	1.13
g-CNF_20%	82.5	4,743	710.9	47.41	57.4	62.5	1.11
Heat-treated							
g-CNF_3%-HT	-	3,450	1,841	465.0	59.3	65.4	0.23
g-CNF_10%-HT	-	4,388	2,507	848.5	59.9	64.2	0.19
g-CNF_20%-HT	-	4,842	2,896	1,198	59.5	65.2	0.17

Where E' = Storage modulus; E'' = Loss modulus; T_{ic} = Temperature of crystalisation start.

Table 5 – Summary of DMA results of 3D printed PLA, CNF10% and g-CNF10% samples with the corresponding effectiveness coefficient and adhesion factor.

Condition	T_{ic} (°C)	E' 25 °C (MPa)	E' 80 °C (MPa)	Max. Tan δ	Effectiveness coefficient (C)	Adhesion factor (A)
PLA	90.7	3,001	1.416	2.94	-	-
CNF10%*	89.7	3,260	15.20	1.54	0.101	-0.418
g-CNF10%	83.2	3,938	30.57	1.13	0.061	-0.573

4. Conclusions

In this work, grafted nanofibrillated cellulose was used to produce reinforced PLA composites for additive manufacturing. Microparticles of PLA with 20 wt% of g-CNF were successfully produced using a Pickering emulsion approach. In comparison with unmodified CNF, the grafting process changed the emulsification behaviour with dissolved PLA resulting in PLA/g-CNF microparticles that incorporated most of the g-CNF that was available in the suspension.

The obtained g-CNF/PLA microparticles were easily processed into filaments and used for 3D printing. The filaments were printed using the same conditions of PLA and did not present any signs of clogging even using a 0.35mm nozzle. The 3D printed composite samples had superior tensile properties than neat PLA, in special if post-printing heat treatment is used. The formulations with high g-CNF content that were heat-treated were dimensionally stable upon PLA crystallisation and also demonstrated improved thermo-mechanical stability, achieving a storage modulus at 60 °C and 80 °C 17 and 850 times higher, respectively, than neat PLA.

We envisage that these microparticles can be used beyond fused deposition modelling. Their attributes are suitable for other conventional manufacturing methods such as injection moulding and compression moulding and can be used for other additive manufacturing methods such as selective laser sintering (under investigation). Although limited reinforcement was achieved, the modification and methodology used in this work enabled the production of PLA composites with high content of CNF, possibly even higher than the content investigated in this work.

Acknowledgements

The authors would like to thank the financial support from the Ministry of Business, Innovation and Employment of New Zealand through, National Science Challenge spearhead project "Additive

manufacturing and 3D and/or 4D printing of bio-composites' [grant 2019-S5-CRS] and The University of Waikato for the development of this paper.

References

[1] J.M. Chacón, M.A. Caminero, P.J. Núñez, E. García-Plaza, I. García-Moreno, J.M. Reverte, Additive manufacturing of continuous fibre reinforced thermoplastic composites using fused deposition modelling: Effect of process parameters on mechanical properties, Compos. Sci. Technol. 181 (2019) 107688. https://doi.org/10.1016/j.compscitech.2019.107688.

[2] G.W. Melenka, B.K.O. Cheung, J.S. Schofield, M.R. Dawson, J.P. Carey, Evaluation and prediction of the tensile properties of continuous fiber-reinforced 3D printed structures, Compos. Struct. 153 (2016) 866–875. https://doi.org/10.1016/j.compstruct.2016.07.018.

[3] C. Gauss, K. Pickering, L.P. Muthe, The use of cellulose in bio-derived formulations for 3D/4D printing: a review, Compos. Part C Open Access. 4 (2021) 100113. https://doi.org/10.1016/j.jcomc.2021.100113.

[4] H. Bi, Z. Ren, R. Guo, M. Xu, Y. Song, Fabrication of flexible wood flour/thermoplastic polyurethane elastomer composites using fused deposition molding, Ind. Crops Prod. 122 (2018) 76–84. https://doi.org/10.1016/j.indcrop.2018.05.059.

[5] Y. Peng, Y. Wu, S. Li, K. Wang, S. Yao, Z. Liu, H. Garmestani, Tailorable rigidity and energy-absorption capability of 3D printed continuous carbon fiber reinforced polyamide composites, Compos. Sci. Technol. 199 (2020) 108337. https://doi.org/10.1016/j.compscitech.2020.108337.

[6] L.P. Muthe, K. Pickering, C. Gauss, A Review of 3D/4D Printing of Poly-Lactic Acid Composites with Bio-Derived Reinforcements, Compos. Part C Open Access. 8 (2022) 100271. https://doi.org/10.1016/j.jcomc.2022.100271.

[7] A. Sharma, M. Thakur, M. Bhattacharya, T. Mandal, S. Goswami, Commercial application of cellulose nano-composites – A review, Biotechnol. Reports. 21 (2019) e00316. https://doi.org/10.1016/j.btre.2019.e00316.

[8] R.J. Moon, A. Martini, J. Nairn, J. Simonsen, J. Youngblood, Cellulose nanomaterials review: structure, properties and nanocomposites, Chem. Soc. Rev. 40 (2011) 3941. https://doi.org/10.1039/c0cs00108b.

[9] F.J. Li, X.T. Yu, Z. Huang, D.F. Liu, Interfacial improvements in cellulose nanofibers reinforced polylactide bionanocomposites prepared by in situ reactive extrusion, Polym. Adv. Technol. 32 (2021) 2352–2366. https://doi.org/10.1002/pat.5264.

[10] S. Sultan, G. Siqueira, T. Zimmermann, A.P. Mathew, 3D printing of nano-cellulosic biomaterials for medical applications, Curr. Opin. Biomed. Eng. 2 (2017) 29–34. https://doi.org/10.1016/j.cobme.2017.06.002.

[11] Q. Wang, C. Ji, J. Sun, Q. Yao, J. Liu, R.M.Y. Saeed, Q. Zhu, Kinetic thermal behavior of nanocellulose filled polylactic acid filament for fused filament fabrication 3D printing, J. Appl. Polym. Sci. 137 (2020) 1–9. https://doi.org/10.1002/app.48374.

[12] D. Filgueira, S. Holmen, J.K. Melbø, D. Moldes, A.T. Echtermeyer, G. Chinga-Carrasco, Enzymatic-Assisted Modification of Thermomechanical Pulp Fibers to Improve the Interfacial Adhesion with Poly(lactic acid) for 3D Printing, ACS Sustain. Chem. Eng. 5 (2017) 9338–9346. https://doi.org/10.1021/acssuschemeng.7b02351.

[13] J. Dong, M. Li, L. Zhou, S. Lee, C. Mei, X. Xu, Q. Wu, The influence of grafted cellulose nanofibers and postextrusion annealing treatment on selected properties of poly(lactic acid) filaments for 3D printing, J. Polym. Sci. Part B Polym. Phys. 55 (2017) 847–855. https://doi.org/10.1002/polb.24333.

[14] H.L. Tekinalp, X. Meng, Y. Lu, V. Kunc, L.J. Love, W.H. Peter, S. Ozcan, High modulus biocomposites via additive manufacturing: Cellulose nanofibril networks as “microsponges,” Compos. Part B Eng. 173 (2019) 106817. https://doi.org/10.1016/j.compositesb.2019.05.028.

[15] D. Rigotti, A. Dorigato, A. Cataldi, L. Fambri, A. Pegoretti, Nanocellulose as reinforcing agent for biodegradable polymers in 3D printing fused deposition modeling, in: ECCM 2018 - 18th Eur. Conf. Compos. Mater., 2020: pp. 24–28.

[16] C.A. Murphy, M.N. Collins, Microcrystalline cellulose reinforced polylactic acid biocomposite filaments for 3D printing, Polym. Compos. 39 (2018) 1311–1320. https://doi.org/10.1002/pc.24069.

[17] L. Li, Y. Chen, T. Yu, N. Wang, C. Wang, H. Wang, Preparation of polylactic acid/TEMPO-oxidized bacterial cellulose nanocomposites for 3D printing via Pickering emulsion approach, Compos. Commun. 16 (2019) 162–167. https://doi.org/10.1016/j.coco.2019.10.004.

[18] Q. Wang, C. Ji, L. Sun, J. Sun, J. Liu, Cellulose nanofibrils filled poly(lactic acid) biocomposite filament for FDM 3D printing, Molecules. 25 (2020). https://doi.org/10.3390/molecules25102319.

[19] T. Ambone, A. Torris, K. Shanmuganathan, Enhancing the mechanical properties of 3D printed polylactic acid using nanocellulose, Polym. Eng. Sci. (2020) 1842–1855. https://doi.org/10.1002/pen.25421.

[20] D. Roy, M. Semsarilar, J.T. Guthrie, S. Perrier, Cellulose modification by polymer grafting: a review, Chem. Soc. Rev. 38 (2009) 2046. https://doi.org/10.1039/b808639g.

[21] A.L. Goffin, J.M. Raquez, E. Duquesne, G. Siqueira, Y. Habibi, A. Dufresne, P. Dubois, From interfacial ring-opening polymerization to melt processing of cellulose nanowhisker-filled polylactide-based nanocomposites, Biomacromolecules. 12 (2011) 2456–2465. https://doi.org/10.1021/bm200581h.

[22] C. Miao, W.Y. Hamad, In-situ polymerized cellulose nanocrystals (CNC)—poly(L-lactide) (PLLA) nanomaterials and applications in nanocomposite processing, Carbohydr. Polym. 153 (2016) 549–558. https://doi.org/10.1016/j.carbpol.2016.08.012.

[23] J. Dong, M. Li, L. Zhou, S. Lee, C. Mei, X. Xu, Q. Wu, The influence of grafted cellulose nanofibers and postextrusion annealing treatment on selected properties of poly(lactic acid) filaments for 3D printing, J. Polym. Sci. Part B Polym. Phys. 55 (2017) 847–855. https://doi.org/10.1002/polb.24333.

[24] S. Gazzotti, H. Farina, G. Lesma, R. Rampazzo, L. Piergiovanni, M.A. Ortenzi, A. Silvani, Polylactide/cellulose nanocrystals: The in situ polymerization approach to improved nanocomposites, Eur. Polym. J. 94 (2017) 173–184. https://doi.org/10.1016/j.eurpolymj.2017.07.014.

[25] J. Gao, F. Bao, D. Wang, R. Ma, S. Jiang, X. Zhang, Y. Yao, X. Han, C. Yan, Facile green ring-opening polymerization of l-lactide catalyzed by natural kaoline, Polym. Chem. 6 (2015) 3083–3089. https://doi.org/10.1039/c5py00102a.

[26] M.A. Ortenzi, L. Basilissi, H. Farina, G. Di Silvestro, L. Piergiovanni, E. Mascheroni, Evaluation of crystallinity and gas barrier properties of films obtained from PLA nanocomposites synthesized via “in situ” polymerization of L-lactide with silane-modified nanosilica and montmorillonite, Eur. Polym. J. 66 (2015) 478–491. https://doi.org/10.1016/j.eurpolymj.2015.03.006.

[27] S. Lee, C.H. Kim, J.K. Park, Improvement of processability of clay/polylactide nanocomposites by a combinational method: In situ polymerization of L-lactide and melt compounding of polylactide, J. Appl. Polym. Sci. 101 (2006) 1664–1669. https://doi.org/10.1002/app.22438.

[28] L. Fang, R. Qi, L. Liu, G. Juan, S. Huang, Synthesis of poly(L-lactide) via solvothermal method, Int. J. Polym. Sci. 2009 (2009). https://doi.org/10.1155/2009/929732.

[29] M. Gestranius, K.S. Kontturi, A. Mikkelson, T. Virtanen, C. Schirp, E.D. Cranston, E. Kontturi, T. Tammelin, Creaming Layers of Nanocellulose Stabilized Water-Based Polystyrene: High-Solids Emulsions for 3D Printing, Front. Chem. Eng. 3 (2021) 1–12. https://doi.org/10.3389/fceng.2021.738643.

[30] Y. Zhang, J. Wu, B. Wang, X. Sui, Y. Zhong, L. Zhang, Z. Mao, H. Xu, Cellulose nanofibril-reinforced biodegradable polymer composites obtained via a Pickering emulsion approach, Cellulose. 24 (2017) 3313–3322. https://doi.org/10.1007/s10570-017-1324-8.

[31] S. Tanpichai, S.K. Biswas, S. Witayakran, H. Yano, Optically transparent tough nanocomposites with a hierarchical structure of cellulose nanofiber networks prepared by the Pickering emulsion method, Compos. Part A Appl. Sci. Manuf. 132 (2020) 105811. https://doi.org/10.1016/j.compositesa.2020.105811.

[32] S. Li, Y. He, Y. Guan, X. Liu, H. Liu, M. Xie, L. Zhou, C. Wei, C. Yu, Y. Chen, Cellulose Nanofibril-Stabilized Pickering Emulsion and in Situ Polymerization Lead to Hybrid Aerogel for High-

Efficiency Solar Steam Generation, ACS Appl. Polym. Mater. 2 (2020) 4581–4591. https://doi.org/10.1021/acsapm.0c00674.

[33] P. Bataille, G. Statioukha, O. Statioukha, Simulation and Optimization of Cellulose and Styrene Graft Copolymerization Process, Can. J. Chem. Eng. 74 (1996) 501–510. https://doi.org/10.1002/cjce.5450740410.

[34] S. Nam, A.D. French, B.D. Condon, M. Concha, Segal crystallinity index revisited by the simulation of X-ray diffraction patterns of cotton cellulose Iβ and cellulose II, Carbohydr. Polym. 135 (2016) 1–9. https://doi.org/10.1016/j.carbpol.2015.08.035.

[35] S. Pilla, S. Gong, E. O'Neill, R.M. Rowell, A.M. Krzysik, Polylactide-pine wood flour composites, Polym. Eng. Sci. 48 (2008) 578–587. https://doi.org/10.1002/pen.20971.

[36] C. Chuensangjun, K. Kanomata, T. Kitaoka, Y. Chisti, S. Sirisansaneeyakul, Surface-Modified Cellulose Nanofibers-graft-poly(lactic acid)s Made by Ring-Opening Polymerization of l-Lactide, J. Polym. Environ. 27 (2019) 847–861. https://doi.org/10.1007/s10924-019-01398-y.

[37] X. Zhao, H. Tekinalp, X. Meng, D. Ker, B. Benson, Y. Pu, A.J. Ragauskas, Y. Wang, K. Li, E. Webb, D.J. Gardner, J. Anderson, S. Ozcan, Poplar as Biofiber Reinforcement in Composites for Large-Scale 3D Printing, ACS Appl. Bio Mater. (2019). https://doi.org/10.1021/acsabm.9b00675.

[38] H. Jing, H. He, H. Liu, B. Huang, C. Zhang, Study on properties of polylactic acid/lemongrass fiber biocomposites prepared by fused deposition modeling, Polym. Compos. 42 (2021) 973–986. https://doi.org/10.1002/pc.25879.

[39] J. Dong, C. Mei, J. Han, S. Lee, Q. Wu, 3D printed poly(lactic acid) composites with grafted cellulose nanofibers: Effect of nanofiber and post-fabrication annealing treatment on composite flexural properties, Addit. Manuf. 28 (2019) 621–628. https://doi.org/10.1016/j.addma.2019.06.004.

[40] S. Bhagia, R.R. Lowden, D. Erdman, M. Rodriguez, B.A. Haga, I.R.M. Solano, N.C. Gallego, Y. Pu, W. Muchero, V. Kunc, A.J. Ragauskas, Tensile properties of 3D-printed wood-filled PLA materials using poplar trees, Appl. Mater. Today. 21 (2020) 100832. https://doi.org/10.1016/j.apmt.2020.100832.

[41] T. Yao, Z. Deng, K. Zhang, S. Li, A method to predict the ultimate tensile strength of 3D printing polylactic acid (PLA) materials with different printing orientations, Compos. Part B Eng. (2019). https://doi.org/10.1016/j.compositesb.2019.01.025.

[42] A. Lanzotti, M. Grasso, G. Staiano, M. Martorelli, The impact of process parameters on mechanical properties of parts fabricated in PLA with an open-source 3-D printer, Rapid Prototyp. J. (2015). https://doi.org/10.1108/RPJ-09-2014-0135.

[43] R. Sood, S.K. Pradhan, Design and development of a low-cost open-source 3D printer and its single response optimization using polylactic acid (PLA) material, in: Mater. Today Proc., 2019. https://doi.org/10.1016/j.matpr.2020.04.905.

[44] A. Ouballouch, L. Lasri, I. Ouahmane, R. El Alaiji, M. Sallaou, S. Ettaqi, Optimization of PLA parts manufactured by the Fused Deposition Modeling Technology, in: 2018 IEEE Int. Conf. Technol. Manag. Oper. Decis. ICTMOD 2018, 2018. https://doi.org/10.1109/ITMC.2018.8691133.

[45] Fused Deposition Modelling of Natural Fibre/Polylactic Acid Composites, J. Compos. Sci. 1 (2017) 8. https://doi.org/10.3390/jcs1010008.

[46] D. Depuydt, M. Balthazar, K. Hendrickx, W. Six, E. Ferraris, F. Desplentere, J. Ivens, A.W. Van Vuure, Production and characterization of bamboo and flax fiber reinforced polylactic acid filaments for fused deposition modeling (FDM), Polym. Compos. 40 (2019) 1951–1963. https://doi.org/10.1002/pc.24971.

[47] H. Liu, H. He, X. Peng, B. Huang, J. Li, Three-dimensional printing of poly(lactic acid) bio-based composites with sugarcane bagasse fiber: Effect of printing orientation on tensile performance, Polym. Adv. Technol. 30 (2019) 910–922. https://doi.org/10.1002/pat.4524.

[48] S. Antony, A. Cherouat, G. Montay, Fabrication and Characterization of Hemp Fibre Based 3D Printed Honeycomb Sandwich Structure by FDM Process, Appl. Compos. Mater. (2020). https://doi.org/10.1007/s10443-020-09837-z.

[49] N. Maqsood, M. Rimašauskas, Characterization of carbon fiber reinforced PLA composites manufactured by fused deposition modeling, Compos. Part C Open Access. 4 (2021). https://doi.org/10.1016/j.jcomc.2021.100112.

[50] Y. Li, S. Gao, R. Dong, X. Ding, X. Duan, Additive Manufacturing of PLA and CF/PLA Binding Layer Specimens via Fused Deposition Modeling, J. Mater. Eng. Perform. (2018). https://doi.org/10.1007/s11665-017-3065-0.

[51] A. Rahimizadeh, J. Kalman, K. Fayazbakhsh, L. Lessard, Recycling of fiberglass wind turbine blades into reinforced filaments for use in Additive Manufacturing, Compos. Part B Eng. (2019). https://doi.org/10.1016/j.compositesb.2019.107101.

[52] N. Yoshiharu, K. Shigenori, W. Masahisa, O. Takeshi, Cellulose microcrystal film of high uniaxial orientation, Macromolecules. 30 (1997) 6395–6397. https://doi.org/10.1021/ma970503y.

[53] P. Tingaut, T. Zimmermann, F. Lopez-Suevos, Synthesis and characterization of bionanocomposites with tunable properties from poly(lactic acid) and acetylated microfibrillated cellulose, Biomacromolecules. 11 (2010) 454–464. https://doi.org/10.1021/bm901186u.

[54] N. Li, Y. Li, S. Liu, Rapid prototyping of continuous carbon fiber reinforced polylactic acid composites by 3D printing, J. Mater. Process. Technol. 238 (2016) 218–225. https://doi.org/10.1016/j.jmatprotec.2016.07.025.

[55] M. Jonoobi, J. Harun, A.P. Mathew, K. Oksman, Mechanical properties of cellulose nanofiber (CNF) reinforced polylactic acid (PLA) prepared by twin screw extrusion, Compos. Sci. Technol. 70 (2010) 1742–1747. https://doi.org/10.1016/j.compscitech.2010.07.005.

[56] J. Dong, C. Mei, J. Han, S. Lee, Q. Wu, 3D printed poly(lactic acid) composites with grafted cellulose nanofibers: Effect of nanofiber and post-fabrication annealing treatment on composite flexural properties, Addit. Manuf. 28 (2019) 621–628. https://doi.org/10.1016/j.addma.2019.06.004.

[57] D. Romanzini, A. Lavoratti, H.L. Ornaghi, S.C. Amico, A.J. Zattera, Influence of fiber content on the mechanical and dynamic mechanical properties of glass/ramie polymer composites, Mater. Des. 47 (2013) 9–15. https://doi.org/10.1016/j.matdes.2012.12.029.

[58] C.A. Correa, C.A. Razzino, E. Hage, Role of maleated coupling agents on the interface adhesion of polypropylene-wood composites, J. Thermoplast. Compos. Mater. 20 (2007) 323–339. https://doi.org/10.1177/0892705707078896.

[59] J.O. Akindoyo, M.D.H. Beg, S. Ghazali, H.P. Heim, M. Feldmann, M. Mariatti, Simultaneous impact modified and chain extended glass fiber reinforced poly(lactic acid) composites: Mechanical, thermal, crystallization, and dynamic mechanical performance, J. Appl. Polym. Sci. 138 (2021) 1–14. https://doi.org/10.1002/app.49752.